Earth and Planetary Science Letters 594 (2022) 117752

Contents lists available at ScienceDirect

Earth and Planetary Science Letters

www.elsevier.com/locate/epsl

Combined dynamical and morphological characterisation of geodynamo simulations

Takashi Nakagawa [a,*], Christopher J. Davies [b]

[a] Department of Earth and Planetary System Science, Hiroshima University, Higashi-Hiroshima 739-8526, Japan
[b] School of Earth and Environment, University of Leeds, Leeds LS2 9JT, United Kingdom

ARTICLE INFO

Article history:
Received 29 December 2021
Received in revised form 1 July 2022
Accepted 23 July 2022
Available online 5 August 2022
Editor: J. Badro

Dataset link: https://doi.org/10.5281/zenodo.6479243

Keywords:
geodynamo
geomagnetic field
force balance
magnetic field morphology

ABSTRACT

Numerical dynamo simulations cannot operate at the physical conditions of Earth's core, yet they often produce fields that appear morphologically similar to the present geomagnetic field. A key issue is therefore to decipher under what conditions "Earth-like" simulations can be achieved. Recent work has shown that a set of simulations undertaken along a specific path in parameter space smoothly approach the QG-MAC dynamics that are expected in Earth's core, whereby the leading order force balance is Quasi-Geostrophic with Magnetic, Archimedean and Coriolis forces equilibrating at first order. However, a systematic link between QG-MAC balance and morphological features of the simulated fields has yet to be established. Here we assess a suite of 67 simulations using established compliance criteria for the field morphology and scale-dependent force balances to quantify the internal dynamics. Morphological compliance with the modern geomagnetic field does not imply a single underlying force balance or vice versa; however, the majority of compliant simulations, including all those approaching a realistic value of the magnetic Reynolds number *Rm*, are in QG-MAC balance. Simulations that simultaneously achieve excellent morphological compliance with Earth's modern field, QG-MAC balance, and high *Rm*, are confined to an intermediate range of dipolarity (the ratio of energy in the dipole field to the energy truncated at degree 12 at the outer boundary). Reversing simulations in this dipolarity range maintain dominant QG-MAC balance during polarity transition, though inertia makes a non-negligible contribution to the force balance.

1. Introduction

Observations of the geomagnetic field obtained at Earth's surface provide a probe into the dynamics and evolution of our planet's deep interior. On long timescales, the field is axial dipole-dominated (Biggin et al., 2020) and exhibits irregular polarity reversals (e.g. Cande and Kent, 1992). However, despite significant recent progress (Panovska et al., 2019), global descriptions of the time-varying field morphology beyond the last 100 kyrs are hindered due to limitations in the spatio-temporal resolution of available data (Korte et al., 2018). The recent field is well characterised by satellite observations over the past 2 decades (e.g. Finlay et al., 2020) and by historical observations over the past 400 years (Jackson et al., 2000). The field morphology over this period, projected down to the core-mantle boundary (CMB), is dominated by two pairs of intense equatorially antisymmetric flux patches at high latitudes situated outside the tangent cylinder and drifting patches at low latitudes in the Atlantic hemisphere. These features are a product of the dynamo process that generates the field in the liquid outer core.

Dynamo simulations provide a powerful tool for inferring links between the observable field at the CMB and the three-dimensional and time-dependent dynamics in Earth's core. The main limitation of these simulations is that they cannot yet employ realistic values of the physical properties of Earth's core (e.g. Wicht and Sanchez, 2019). Recent simulations have reached extreme conditions of low viscosity, rapid rotation and vigorous convection (e.g., Sheyko et al., 2016) and it has been argued that these may already represent the large-scale dynamics expected in Earth's core (e.g., Aubert et al., 2017). However, these simulations are scarce (the vast major of existing simulations use much more modest physical properties), and computationally expensive such that a systematic exploration of parameters at such extreme conditions is unlikely in the near future. Moreover, there is no guarantee that any given set of input parameters will produce a CMB field that resembles the modern geomagnetic field. A crucial question is therefore to establish how an Earth-like magnetic field morphology can be achieved.

---

[*] Corresponding author.
E-mail address: takashi.geodynamics@gmail.com (T. Nakagawa).

https://doi.org/10.1016/j.epsl.2022.117752

In order to determine if a numerical dynamo simulation can be considered as "Earth-like", two approaches are currently used. The first is to compare the magnetic field derived from numerical dynamo simulations to models of the observed field (Dormy et al., 2000; Christensen et al., 2010; Davies and Constable, 2014; Mound et al., 2015). We follow previous studies (Aubert et al., 2013; Davies and Constable, 2014; Mound et al., 2015; Christensen, 2018; Gastine et al., 2020) and employ the compliance criteria of Christensen et al. (2010), which determine the misfit between simulated and observed fields in terms of their axial dipole dominance, zonality, equatorial symmetry, and flux concentration factor (FCF). Christensen et al. (2010) suggested that acceptable misfits are obtained in a wedge-shaped region of the parameter space defined by the magnetic Reynolds number Rm, the ratio of magnetic advection and diffusion timescales, and E/Pm, the ratio of magnetic diffusion and rotational timescales where E is the Ekman number and Pm is the magnetic Prandtl number. However, Davies and Constable (2014) and Tassin et al. (2021) have found that simulations with E/Pm and Rm within the wedge may not produce simulated field morphologies with acceptably low misfit as defined by Christensen et al. (2010). Moreover, the compliance criteria only test the CMB field that is produced by the simulation; they do not consider the internal state of the dynamo.

The second method for assessing dynamo simulations is to compare the force balance output from the model against theoretical predictions (e.g. Davidson, 2013; Yadav et al., 2016; Aubert et al., 2017). In Earth's core, plausible values for the material properties strongly suggest that viscous and inertia forces are unimportant for the bulk dynamics. Recent high-resolution simulations (e.g., Aubert et al., 2017) have found that the large-scale force balance is quasi-geostrophic (QG) at leading order. At first order the expected balance is between Magneto-Archimedean-Coriolis (MAC) forces (Davidson, 2013; Aubert et al., 2017), and hence the dynamo is in QG-MAC balance. Schwaiger et al. (2019) surveyed a wide parameter range and found that dipole-dominated dynamos are generally in QG-MAC balance, while dynamos where the Lorentz force is replaced at first order by viscosity (QG-VAC balance) or inertia (QG-CIA balance) occur only near the onset of convection or when the CMB field loses dipole-dominance. Aubert et al. (2017) co-varied E, Pm and the convective forcing in simulations that follow a path determined by enforcing QG-MAC balance and invariance of Rm. Moving along the path towards Earth-like conditions they found increasing ratios of magnetic to kinetic energy and ohmic to viscous dissipation, which are expected on theoretical grounds (Davidson, 2013). Davies et al. (2022) pointed out that QG-MAC theory smoothly links the root-mean-square (RMS) magnetic field strength both in the bulk and at the CMB as well as the CMB dipole field strength between simulations and estimates for present-day Earth. However, while some QG-MAC dynamos have been shown to exhibit Earth-like magnetic fields according to the compliance test (Aubert et al., 2013, 2017), a systematic link between the dynamo dynamics, as measured by the force balance, and the observed field morphology, as measured by the compliance criteria, has yet to be established.

In this paper, we develop a direct link between the dynamo force balance and the observational field. A total of 67 simulations are used: 48 new cases and 19 cases from previous work (Mound et al., 2015; Sprain et al., 2019; Biggin et al., 2020; Meduri et al., 2021). Detailed analysis of these simulations is supplemented by literature data from Schwaiger et al. (2019). The new cases are produced by first extending the simulated path of Aubert et al. (2017) to larger values of E and Pm and then perturbing the input parameters about those suggested by the path theory. This allows us to simulate a range of dynamical behaviour without systematically sampling regions of parameter space that yield the QG-VAC balance, which is not relevant for Earth's core. We address the following questions: 1) What is the relationship between force balances and the morphological semblance with the modern geomagnetic field? 2) Can we determine conditions that produce Earth-like field morphology (as defined by the compliance criteria) and force balance (assumed to be QG-MAC) and relate these to input parameters for dynamo simulations? Finally, given that polarity reversals are a fundamental characteristic of the geomagnetic field, we briefly consider the behaviour of reversing simulations that produce both an Earth-like dipolarity (the ratio of dipole magnetic energy to magnetic energy up to spherical harmonic degree 12 on the outer boundary), Rm, and force balance.

2. Model description

2.1. Numerical dynamo simulations

We numerically solve the Boussinesq equations of the magnetohydrodynamic dynamo in a rotating spherical shell using the code described in Willis et al. (2007) and Davies et al. (2011). Details of the numerical model are given in the supplemental material. The non-dimensional numbers are

$$Ra^* = \frac{g\alpha F}{8\pi\rho\kappa^2\Omega} \tag{1}$$

$$Pr = \frac{\nu}{\kappa} \tag{2}$$

$$Pm = \frac{\nu}{\eta} \tag{3}$$

$$E = \frac{\nu}{2\Omega D^2} \tag{4}$$

where F is the total co-density flux, ρ is the density, κ is the co-density diffusivity, η is the magnetic diffusivity, Ω is the angular velocity of planetary rotation, $D = r_o - r_i$ is the thickness of the spherical shell where r_o denotes the outer boundary and r_i the inner boundary, ν is the fluid viscosity, g is the gravitational acceleration at the CMB and α is the co-density expansivity. The ratio of inner to outer radii is set to 0.35 throughout.

Two series of numerical simulations are performed: (1) pure thermal driving and (2) thermo-chemical driving. In pure thermally driven cases, the boundary conditions are fixed flux ($F_i = -1/r_i^2$ and $F_o = -1/r_o^2$) and there is no source-sink term because we assume no radioactive heating or secular cooling (Davies and Gubbins, 2011). A few cases include a heterogeneous outer boundary condition with amplitude (ε_q) given as:

$$\varepsilon_q = \frac{F_{max} - F_{min}}{F_o}, \tag{5}$$

where F_o is the heat flow across the outer boundary, F_{max} is the maximum boundary heat flow and F_{min} is the minimum boundary heat flow. The pattern of heterogeneity is taken from the tomographic model of Masters et al. (2000).

For thermo-chemically-driven cases, we follow Aubert et al. (2013). The mean co-density flux at the outer boundary is zero, while the amplitude of the (purely thermal) outer boundary heterogeneity is modelled by using $\Delta q = 1.5 q_{ad}$ and an adiabatic heat flow of $q_{ad} = 11$ TW in Eq. (5) of Aubert et al. (2013), with the same pattern as the thermal cases:

$$\frac{\Delta F_c}{F_o} = \frac{\alpha}{C_p}\left(\frac{r_i}{r_o}\right)^2\left(\frac{\overline{\psi} - \psi_i}{\varepsilon_L + \varepsilon_B}\right)\frac{\Delta q}{q_{ad}} \sim 0.13 \tag{6}$$

where ΔF_c is the peak-to-peak amplitude of co-density heterogeneity, c_p is the heat capacity, $\overline{\psi} - \psi_i \sim 10^7$ is the difference of gravitational potential between the inner core boundary and the average outer core value, and $\varepsilon_L + \varepsilon_B \sim 0.2$ is the combined thermodynamic efficiency of latent heat and light element release. The mean co-density flux at the inner boundary is $1/r_i^2$ without imposing the lateral heterogeneity. The source-sink term of co-density flux is (Christensen and Wicht, 2008)

$$S = -\frac{3}{r_o^3 - r_i^3}. \tag{7}$$

Eq (7) also gives the ratio of thermal and chemical buoyancy flux, which is 86 percent chemical driving by using the non-dimensional radii at inner and outer spheres.

2.2. Data analysis

For the output diagnostics, the magnetic Reynolds number (Rm) and the ratio of magnetic and kinetic energies (M) are used here, given as:

$$Rm = \frac{UD}{\eta} \tag{8}$$

$$M = \frac{E_M}{E_K} \tag{9}$$

where U is the characteristic fluid velocity based on the RMS (Root-Mean-Square) kinetic energy, E_K is the kinetic energy, and E_M is the magnetic energy. The magnetic Reynolds number in Earth's core ranges from 400 to 4000 (Aubert et al., 2017). Here, we use $\langle Rm \rangle = 500$ as the threshold for an Earth-like magnetic Reynolds number based on the minimum constraints from the core surface flow model (e.g., Holme, 2015), where $\langle \ldots \rangle$ denotes the time-averaged value.

In order to estimate the relevant force balance in numerical dynamo simulations, we compute the spectrum of each force as a function of radius following Aubert et al. (2017) and Schwaiger et al. (2019):

$$F_i^2(r) = \sum_{l=0}^{lmax} F_{i,l}^2(r) = \sum_{l=0}^{lmax} \sum_{m=0}^{l} F_{i,lm}^2(r) \tag{10}$$

where $F_{i,lm}$ is the spectral form of each force (i = V: viscous; i = I: inertia; i = L: Lorentz; i = C: Coriolis; i = B; buoyancy; i = P: pressure) and l_{max} is the maximum truncation degree of spherical harmonic order in the numerical dynamo simulations. The force balance spectra across the bulk fluid layer are obtained by integrating Eq. (10) radially, excluding the viscous boundary layers at the top and bottom of the fluid layer (Aubert et al., 2017). The thickness of the viscous boundary layers, d_ν, is defined by the peaks in the radial profile of horizontal velocity near the boundary (King et al., 2013). The forces are analysed as a function of spherical harmonic degree l rather than order m as explained in Aubert (2019).

Using equation (10), we can define quantities that directly measure the force balance, following Schwaiger et al. (2019). First, the strong-fieldness δ quantifies the amplitude difference between the Lorentz force and the larger of the viscous and inertial forces:

$$\delta = \left(\frac{\sum_{l=1}^{l_{max}} F_{L,l}^2}{\sum_{l=1}^{l_{max}} \max(F_{I,l}^2, F_{V,l}^2)} \right)^{\frac{1}{2}}. \tag{11}$$

Larger δ indicates a larger disparity between Lorentz force and both inertial and viscous effects, and hence a greater adherence to QG-MAC balance. Second, χ_{norm} represents the difference between the scale $l_{pol}(r) = \max(E_{K,l}(r))$ at which the poloidal kinetic energy spectrum $E_{K,l}(r)$ peaks and the scale l_{MAC} at which QG-MAC balance is achieved, normalised by the minimum difference between l_{pol} and the scales l_{VAC} and l_{CIA} at which VAC and CIA balance are achieved:

$$\chi_{norm} = \frac{\chi_{MAC}}{\min(\chi_{CIA}, \chi_{VAC})} \tag{12a}$$

where

$$\chi_i = \left(\frac{4\pi}{V} \int_{r_i+d_v}^{r_o-d_v} \left(\frac{l_{pol}(r) - l_i(r)}{l_{pol}(r)} \right)^2 r^2 dr \right)^{\frac{1}{2}}. \tag{12b}$$

Here $l_i(r)$ is the crossing degree of two force spectra ($i =$ MAC: Lorentz and buoyancy; $i =$ CIA: inertia-buoyancy; $i =$ VAC: Viscous-buoyancy) defined in Eqs. (16) to (18) in Schwaiger et al. (2019). Based on the results of Schwaiger et al. (2019), we expect that lower χ_{norm} indicates that the characteristic flow scale approaches l_{MAC} and diverges from the scales where either VAC or CIA balances dominate.

Both δ and χ_{norm} are direct measures of the dominant force balance in the dynamo, while M is a convenient proxy for the ratio of Lorentz and inertial forces that is easier to calculate and more commonly output in dynamo simulations. Here we will compare the three quantities directly. The QG-MAC balance is approached when $\langle \delta \rangle > 1$, $\langle \chi_{norm} \rangle < 1$ and $\langle M \rangle > 1$ (Schwaiger et al., 2019). Unless otherwise stated, all derived quantities (e.g. energies, force balance, etc) are computed at each time point before averaging over time.

In reversing simulations, it is important for consistency to compute force balance spectra over stable and transitional periods separately. We define stable polarity periods as times when the magnitude of the dipole tilt angle ($-90 \le \theta_{dip} \le 90$) exceeds 45 degrees. Our focus is on times of stable polarity, which we analyse in section 3.1. In section 3.2 we briefly consider reversing behaviour in the QG-MAC regime.

For assessing how numerical dynamo simulations resemble the observed geomagnetic field, we use the criteria proposed by Christensen et al. (2010). This test is composed of computing misfit based on four quantities: axial dipole dominance, AD/NAD; odd-even ratio, O/E; zonality, Z/NZ; and flux concentration factor, FCF. Those values are computed with the gauss coefficients truncated at spherical harmonic degree 8. The misfit of each parameter is computed as:

$$\chi_i^2 = \left(\frac{\ln \Pi_i - \ln \Pi_i^M}{\ln \Pi_i^S} \right)^2 \tag{13}$$

where Π_i are the computed values of each criterion ($i = AD/NAD$, O/E, Z/NZ, FCF), Π_i^M is the corresponding value for the geomagnetic field, and Π_i^S is the standard deviation estimated from time-dependent and statistical field models (see Table 2 in Christensen et al., 2010). Based on the total misfit $\chi^2 = \sum_i \chi_i^2$, simulations are categorized as excellent ($\chi^2 \le 2$), good ($2 < \chi^2 \le 4$), marginal ($4 < \chi^2 \le 8$) or non-compliant ($\chi^2 > 8$).

The original compliance criteria were applied by averaging each misfit measure over approximately 30 advection times, corresponding to around 5000 yrs (Christensen et al., 2010). Mound et al. (2015) showed that the individual χ_i^2 can vary substantially over the duration of a simulation and so care is needed when comparing to the modern geomagnetic field. In order to do that, we compute χ^2 at each time point and then average over time windows over different lengths (excluding the initial transient). We divide the time-series into N windows of equal length and focus on windows of 400 years, the length of the historical record, but also consider other window lengths. Finally, the total misfit is quoted for the window where χ^2 takes its minimum value. This procedure for choosing an 'optimum' window reflects the fact that

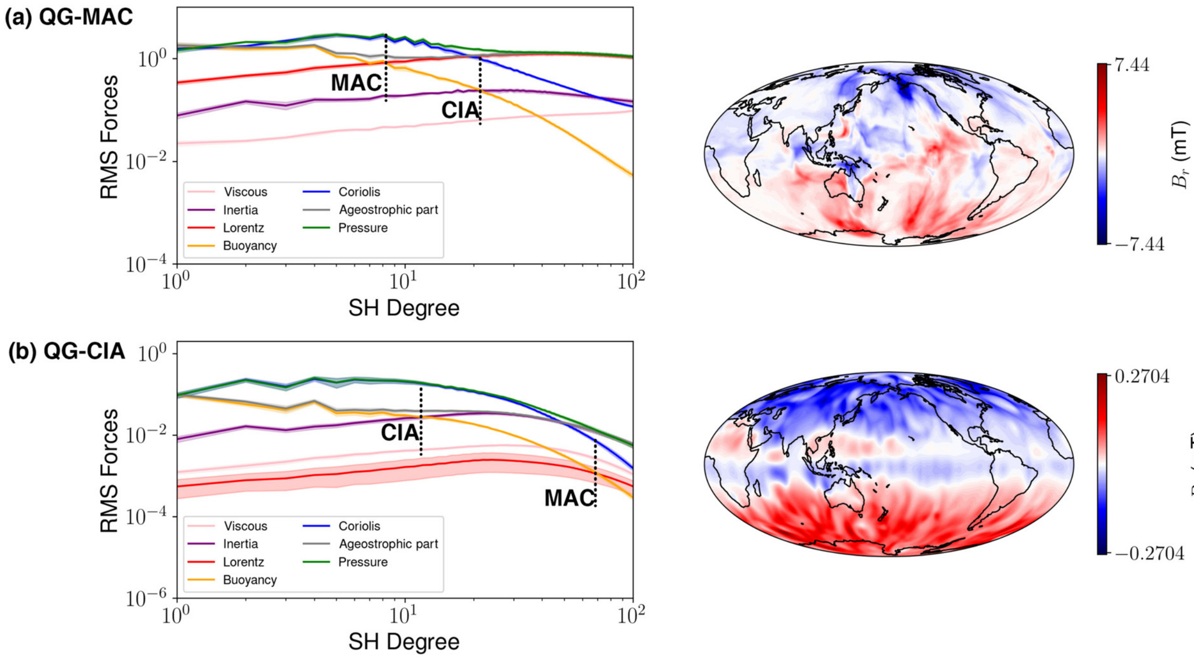

Fig. 1. Force balance spectra (left) and radial magnetic field at the CMB (right) for (a) QG-MAC dynamo (LEDT042) and (b) QG-CIA dynamo (LEDT047). Vertical dashed lines indicate the spherical harmonic degree of the force balance (MAC: QG-MAC; CIA: QG-CIA). The case number can be referred to the Table S1 (Excel spreadsheet). (For interpretation of the colours in the figure(s), the reader is referred to the web version of this article.)

time in the simulation is arbitrary, hence, any 400-yr window can be tested against the observed field.

As a final measure of the surface field morphology, we compute the dipolarity f_{dip}, defined as the ratio of the RMS CMB dipole field strength to the RMS strength of the CMB field truncated up to degree 12 (Christensen and Aubert, 2006). Davies et al. (2022) argued that, over the timescales spanned by dynamo simulations, the value of $\langle f_{dip} \rangle$ for the geomagnetic field should lie in the range 0.35–0.75. This range encompasses the values of 0.64 and 0.7 ± 0.3 for the satellite and historical fields respectively, rules out weakly and viscously-controlled dynamos that produce anomalously high f_{dip}, and also omits dynamos that are clearly in the multipolar regime (Christensen and Aubert, 2006).

3. Results

We calculate compliance criteria and force balance spectra for 48 new simulations (37 purely thermally-driven and 11 thermo-chemically-driven) plus 19 (all pure thermally-driven) previously published simulations (Mound et al., 2015; Sprain et al., 2019; Biggin et al., 2020; Meduri et al., 2021). A case summary is provided in the supplemental material (Table S1). Briefly, the input parameters are $120 \le Ra^* \le 2400$, $0.78125 \le Pm \le 50$ and $7.8125 \times 10^{-6} \le E \le 10^{-3}$. Fourteen of these cases (LEDT001 to LEDT007 and LEDT038 to LEDT044) are designed to approximately follow the path theory of Aubert et al. (2017), in which the parameters are defined such that

$$Ra_F = \epsilon Ra_{F0}; \quad \frac{E}{Pm} = \sqrt{\epsilon}\frac{E_0}{Pm_0}. \tag{14}$$

Here ϵ is the path parameter, Ra_F is the flux Rayleigh number $Ra_F = Ra^*(E/Pr)^2$, and we set $E_0 = 1 \times 10^{-3}$ (reference Ekman number) and $Pm_0 = 50$ (reference magnetic Prandtl number). By using the relationship between flux Rayleigh number and modified Rayleigh number with $Pr = 1$, the modified Rayleigh number has the relationship: $Ra^* = \epsilon^{-1} Ra_0^*$ where $Ra_0^* = 120$ is the reference modified Rayleigh number. The other 32 cases randomly select the input parameters within the range shown above.

All simulations use a spatial resolution from 96 to 192 radial grid points and truncation of up to 96 to 128 spherical harmonic degree, depending on the combination of input parameters. Time integrations are performed for between 100 and 10000 advection times ($t_{adv} = t'D/U$), where an Earth-like advection time is around 150 yrs (Christensen et al., 2010). This time integration period spans Holocene to Myr timescales, which is sufficient to compare outputs to the modern geomagnetic field. Several simulations include polarity reversals, which are monitored by using the dipole tilt angle. To ensure consistency between non-reversing and reversing cases, we avoid taking averages over times including polarity reversals.

3.1. Relationship between field morphology and force balance

Fig. 1 shows the force balance spectra in the bulk fluid for typical cases that represent the QG-MAC (LEDT042) and QG-CIA (LEDT047) regimes. Also shown are maps of the radial magnetic field B_r at the outer boundary of the simulation from the 400-yr window with minimum value of total misfit of compliance criteria. In the QG-MAC dynamo (Fig. 1a), the ordering of the forces is the same as obtained by Schwaiger et al. (2019) and Aubert (2019, Fig. 2) whose terminology we follow. At leading order, geostrophic balance occurs at low harmonic degrees and is replaced by a magnetostrophic balance at high degree. At first order the MAC balance is achieved at spherical harmonic degree $l_{MAC} \sim 10$; below this scale the (vorticity) balance is characterised by a thermal wind, while above this scale a magnetic wind prevails. Inertial effects balance buoyancy and what remains of the Coriolis effect at harmonic degree $l_{CIA} \sim 20$. The separation between Lorentz and inertial forces is around 1 order of magnitude at the large scales, which is lower than the scale separation that arises at lower E/Pm (e.g., Aubert, 2019). This simulation provides a good match to the modern geomagnetic field, with a dominantly dipolar and equatorially anti-symmetric field including intense high-latitude flux patches. In the QG-CIA dynamo (Fig. 1b), the zeroth and first order balances are the same as found by Schwaiger et al. (2019), with some differences emerging at smaller scales. In particular, the ex-

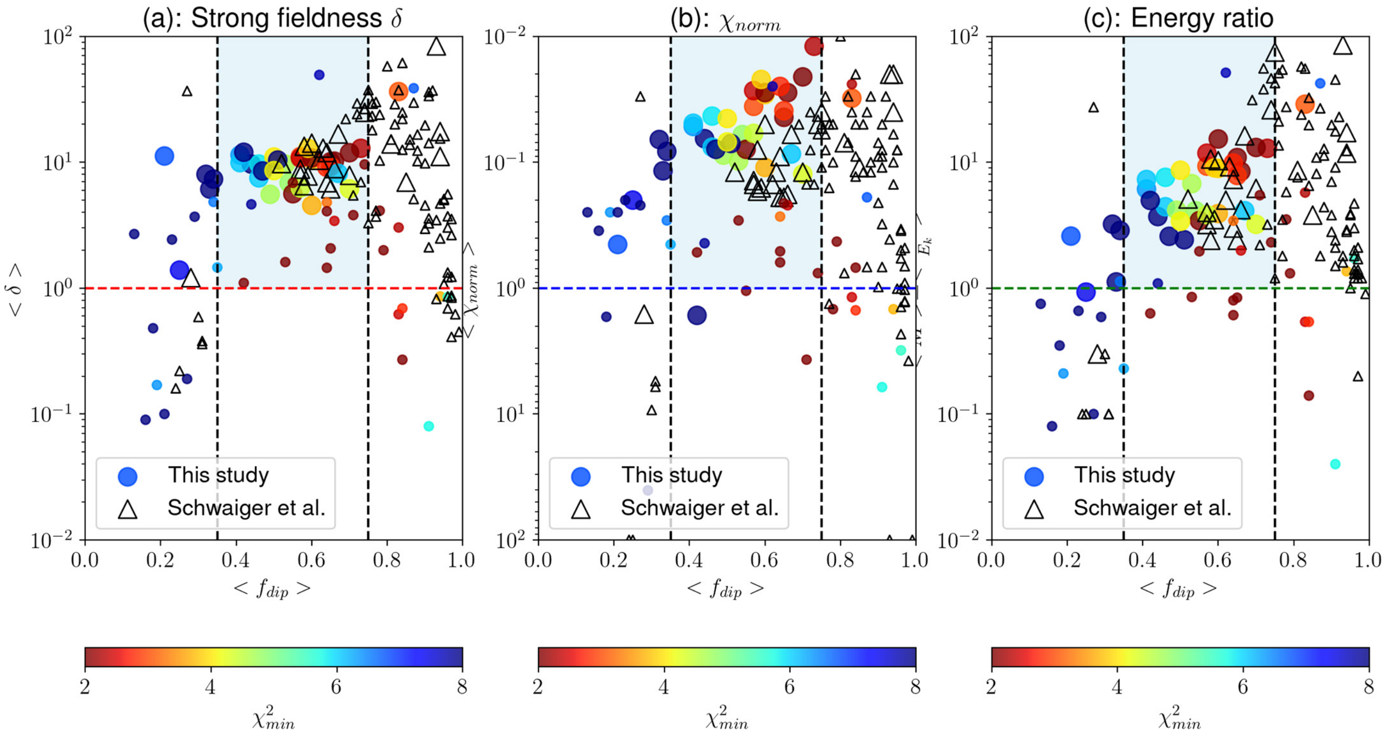

Fig. 2. Time-averaged strong-fieldness $\langle\delta\rangle$ (a), misfit value between the characteristic lengthscale of kinetic energy production and the force balance lengthscales $\langle\chi_{norm}\rangle$ (b), and energy ratio $\langle M\rangle$ of force balance spectra (c) all as a function of time-averaged dipolarity $\langle f_{dip}\rangle$. The filled colour denotes the total misfit value of the compliance test taken at the time window where χ^2 reached its minimum value. The open triangle symbols are taken from the literature data in Schwaiger et al. (2019). The large symbols correspond to $\langle Rm\rangle \geq 500$ and small symbols correspond to $\langle Rm\rangle < 500$. $\langle\ldots\rangle$ denotes the time-averaged value.

ample in Fig. 1b achieves QG-VAC balance around $l_{VAC} = 50$ before achieving a QG-MAC balance at higher degrees, while the example in Schwaiger et al. (2019) does not achieve QG-VAC or QG-MAC balance at any spherical harmonic degree. The surface field for this case is strongly dipolar (high f_{dip}) and does not comply with the morphology of the geomagnetic field. We have found another branch of the QG-CIA dynamo with low f_{dip} (see below), but the spectra show that the ordering of the force balances is the same between the two cases.

Fig. 2 shows $\langle\delta\rangle$, $\langle\chi_{norm}\rangle$, and $\langle M\rangle$, all evaluated in the bulk fluid, as a function of $\langle f_{dip}\rangle$ with the colour bar indicating the value of χ^2 in the 400-yr window corresponding to a minimum χ^2. Literature data taken from Schwaiger et al. (2019) is also plotted. QG-MAC balance arises when $\langle\delta\rangle > 1$, $\langle M\rangle > 1$, $\langle\chi_{norm}\rangle < 1$ as shown by the dashed lines and is more strongly enforced as $\langle\delta\rangle$ and $\langle M\rangle$ increase above 1 and as $\langle\chi_{norm}\rangle$ decreases below 1. The blue shaded region delineates the simulations that produce both global QG-MAC balance and $0.35 \leq \langle f_{dip}\rangle \leq 0.75$.

Four main findings emerge from Fig. 2. First, morphological compliance with the modern geomagnetic field does not imply a single underlying force balance: low χ^2 values are obtained in both QG-MAC and QG-CIA regimes. However, the low χ^2 QG-CIA models appear close to the transition to QG-MAC, generally have low Rm, and produce either too low or too high $\langle f_{dip}\rangle$ compared to modern Earth. Therefore, these simulations are not representative of Earth's core dynamo. Second, QG-MAC balance does not imply low χ^2. In particular, QG-MAC cases with high and low $\langle f_{dip}\rangle$ provide poor agreement with Earth's modern field and are not guaranteed to yield high Rm. Third, the two previous findings do not appear to be affected by the degree to which a single force balance dominates. For example, increasing δ, χ_{norm}^{-1} or M (i.e. greater adherence to QG-MAC balance) does not produce a systematic trend in χ^2. Finally, there appears to be a range of $\langle f_{dip}\rangle$ that is broadly consistent with the range suggested independently by Davies et al. (2022) in which the majority of simulations are characterized by QG-MAC balance, good or excellent morphological semblance, and high Rm. Remarkably, the single parameter $\langle f_{dip}\rangle$ appears to provide a reasonable proxy for all three of these desirable characteristics.

To assess the effect of averaging on χ^2, Fig. 3 plots $\langle\delta\rangle$ (evaluated in the bulk fluid) as a function of $\langle f_{dip}\rangle$ with the colour bar indicating the minimum value of χ^2 obtained with no time windowing, and time windowing spanning 400 years, 1000 years, and the total length of the simulation. In all four cases, the individual compliance criteria are computed at each time step before averaging, as in Christensen et al. (2010). χ^2 increases with the length of averaging, which is expected because the simulated field morphologies vary significantly over timescales greater than the historical period. Large temporal variations in χ^2 have previously been found in both dynamo simulations (Mound et al., 2015) and time-dependent field models spanning the period 10-100 ka (Panovska et al., 2019); indeed, the need for appropriate averaging when applying the compliance criteria was recognised in the original study by Christensen et al. (2010). After 1000 yrs of averaging we observe a roughly equal partitioning between dipolar models ($\langle f_{dip}\rangle > 0.35$) with good/excellent compliance and those with marginal/poor compliance, similar to results in Christensen et al. (2010) for the case of a fixed flux outer boundary. When averaged over their whole duration, most simulations display marginal or non-compliance with the modern geomagnetic field. Nevertheless, on millennial and sub-millennial timescales Fig. 3 shows that the main features identified in Fig. 2 are preserved.

3.2. Preliminary links to polarity reversals

Polarity reversals are a fundamental characteristic of geomagnetic secular variation (e.g., Valet and Fournier, 2016) and should therefore be represented in any Earth-like dynamo model. The large computational costs required to simulate the long time-scales associated with reversals (and other diagnostics of paleomagnetic

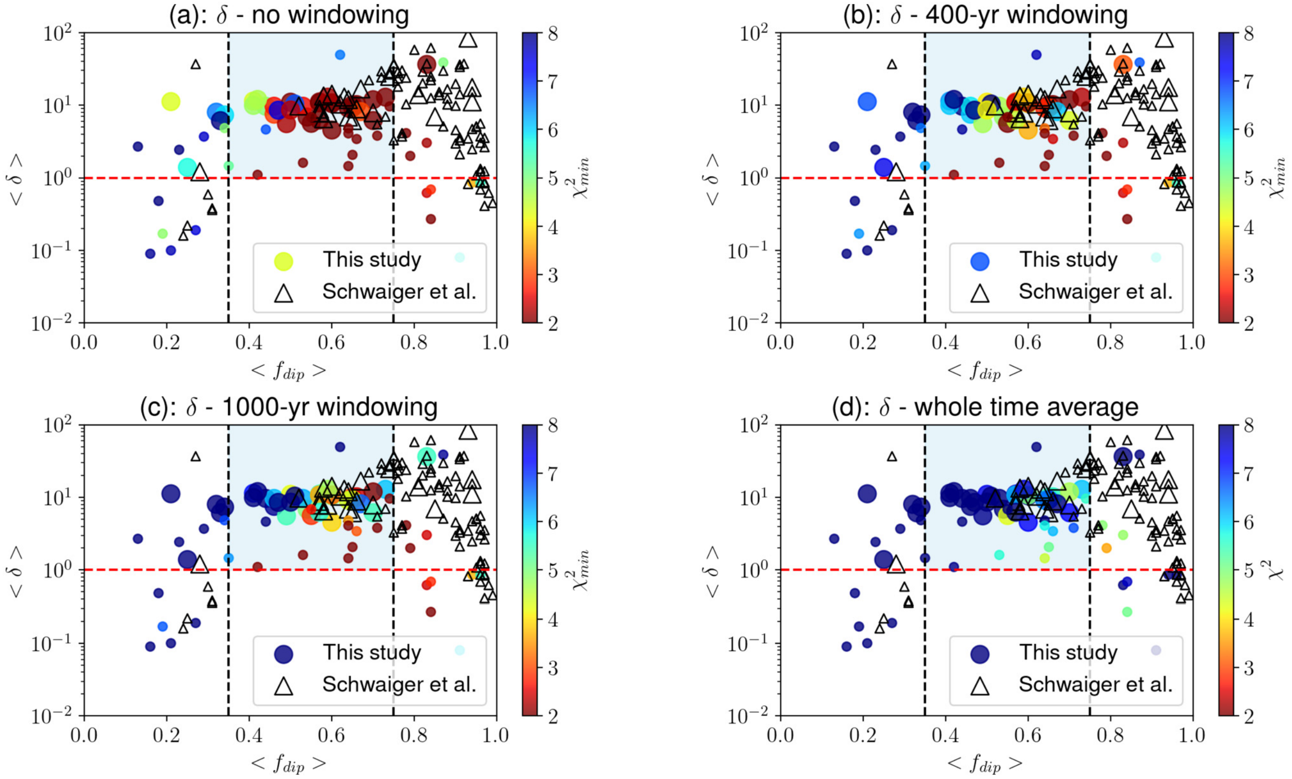

Fig. 3. Effect of time-window length on χ^2 as a function of strong fieldness δ and dipolarity f_{dip}. (a) no time windowing; (b) 400-yr time windowing; (c) 1000-yr time windowing, (d) whole time-averaged value (Same procedure as Christensen et al., 2010). Filled colour indicates the total misfit of compliance criteria (see Table S1). Circle: This study (Large: $Rm \geq 500$; Small: $Rm < 500$); Triangle (Size criterion is the same as Circle): Schwaiger et al. (2019). Shaded region shows the range of $\langle f_{dip} \rangle$ suggested by Davies et al. (2022).

field behaviour) mean that it is currently not feasible to undertake the systematic analysis presented in Section 3.1 above using only reversing simulations. Nevertheless, it is important to identify whether the intermediate $\langle f_{dip} \rangle$ regime in Fig. 2 contains reversing dynamos and, if so, the behaviour of the force balance during the reversal. Our simulation suite contains 5 reversing simulations that maintain QG-MAC balance and $0.35 \leq \langle f_{dip} \rangle \leq 0.75$ (Table S1), but none of these also satisfy both high $Rm(\sim 1000)$ and a good or excellent ($\chi^2 < 4$) compliance with the modern field morphology on 100–1000 year timescales. We focus on the case LEDT002, which has $Rm = 1185$ but does not achieve $\chi^2 < 4$ in any window of $\geq$400 years, though it does achieve $\chi^2 = 4.95$ at a single instant in time.

Fig. 4 shows the time variations of the energy ratio M, dipolarity f_{dip}, and dipole tilt angle as a function of time. Fig. 3a shows that M remains above 2 for the whole duration of the simulation, indicating that both the stable and transitional dynamo are likely to be in QG-MAC balance. On the other hand, M is reduced during transitions compared to times of stable polarity, suggesting an increased role of inertia during the reversal. The variations in M are due to a decrease in the magnetic energy, while kinetic energy remains relatively constant in time. The strong-fieldness δ remains relatively stable and larger than 7 through the reversal, while χ_{norm} is generally below 0.1 aside from a handful of instantaneous 'spikes' where it reaches $O(1)$ (see Fig. 5). Reversals (seen by the tilt angle of dipole latitude in Fig. 4b) also correspond to times of smaller f_{dip} (Fig. 4a), which is consistent with previous studies (e.g., Menu et al., 2020). The decrease in f_{dip} arises due to a strong decrease in the energy of dipole field, though the energy of the whole outer boundary field also drops during the reversal, consistent with the overall decrease in magnetic energy.

Fig. 6 shows force balance spectra and the radial magnetic field at the outer boundary taken at selected times before, during and after the polarity reversal in Fig. 4. The force balance spectra (left of Fig. 6), show that the relative ordering of the forces is preserved through the reversal. The field morphology (right of Fig. 6 directly before and after the reversal is dipole-dominated, but not well-compliant with the modern geomagnetic field (see Table S1); however, any such agreement would perhaps be coincidental since the current geomagnetic field has remained in stable polarity for over 700 kyrs and shows no clear signs of reversing.

To further investigate the reversing dynamo behaviour, Fig. 7 shows the ratio of Lorentz to inertial force spectra, $F_{I,l}/F_{L,l}$, as a function of time spanning the reversal shown in Fig. 4. During the reversal this ratio is increased to $\sim$0.3 to 0.4 across the largest scales $l \approx 1-10$, which is consistent with the results of Tassin et al. (2021) who considered the force balance at the scale l_{pol}. The RMS amplitude of the Lorentz force (not shown) drops by about a factor of 1.5 between the times t_1 to t_2 and so we suspect that the change in F_I/F_L is predominantly due to a weakening of the Lorentz force preceding the main phase of the reversal rather than an increase in the strength of the inertial term. This view is supposed by the observation that magnetic energy changes more than kinetic energy between t_1 and t_2. Therefore, while this dynamo remains in QG-MAC balance according to the definition based on M, this balance is significantly perturbed by inertial effects. Tassin et al. (2021) argue that this inertia force elevation would not be likely to arise in Earth's core, which seems plausible given current theoretical understanding of the dynamo (Davidson, 2013) but is impossible to probe directly for Earth's core because the large-scale force spectrum is unobservable. In any case, the purpose here is simply to show that reversing dynamos exist in the region of parameter space where QG-MAC balance, high Rm and Earth-like f_{dip} are simultaneously achieved (blue shaded region in Fig. 2). A large suite of reversing dynamos that sample this regime will help to elucidate the role of inertia in governing polarity changes.

(a) Energy ratio and dipolar fraction

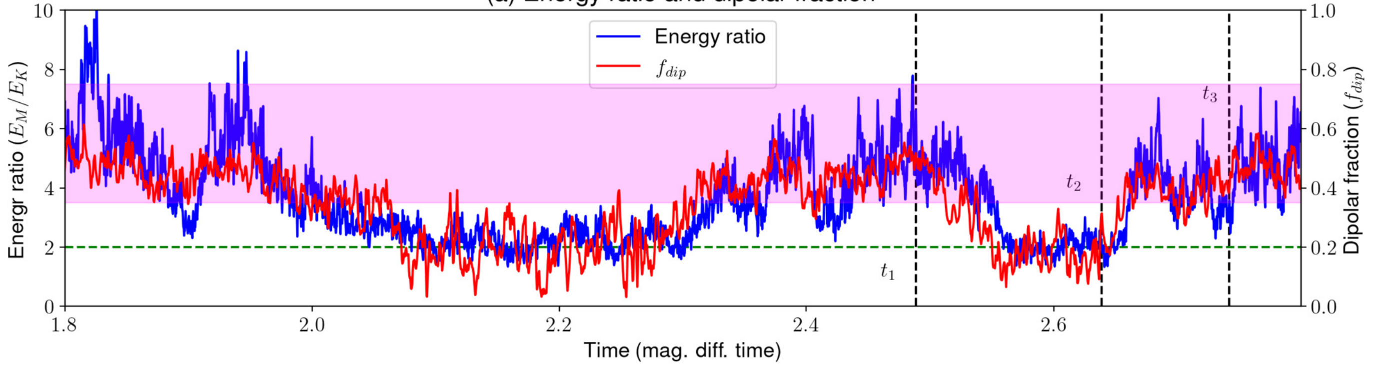

(b) Dipole tilt angle

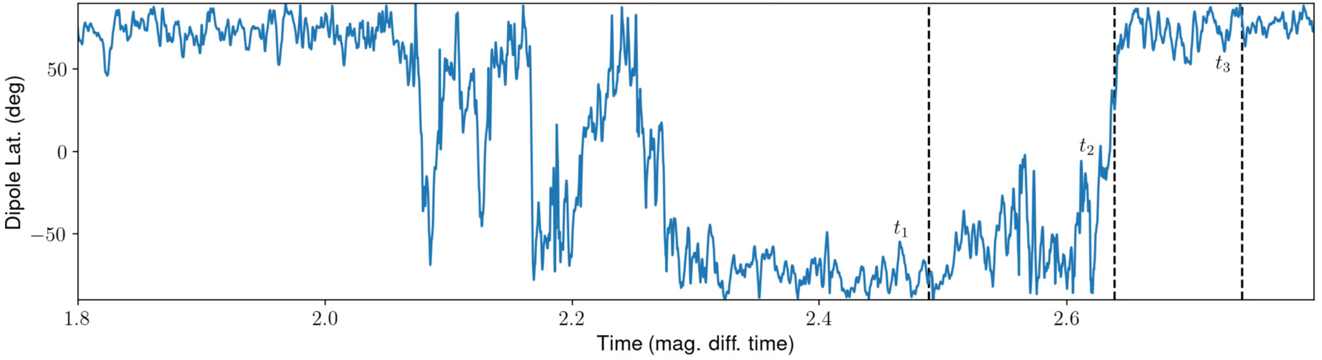

Fig. 4. Energy ratio of magnetic to kinetic energy M and dipole fraction f_{dip} (a) and dipole tilt angle (b) as a function of time for the simulation LEDT002 (see Table S1). Time t_1: Before the reversal, t_2: During the reversal and t_3: After reversal.

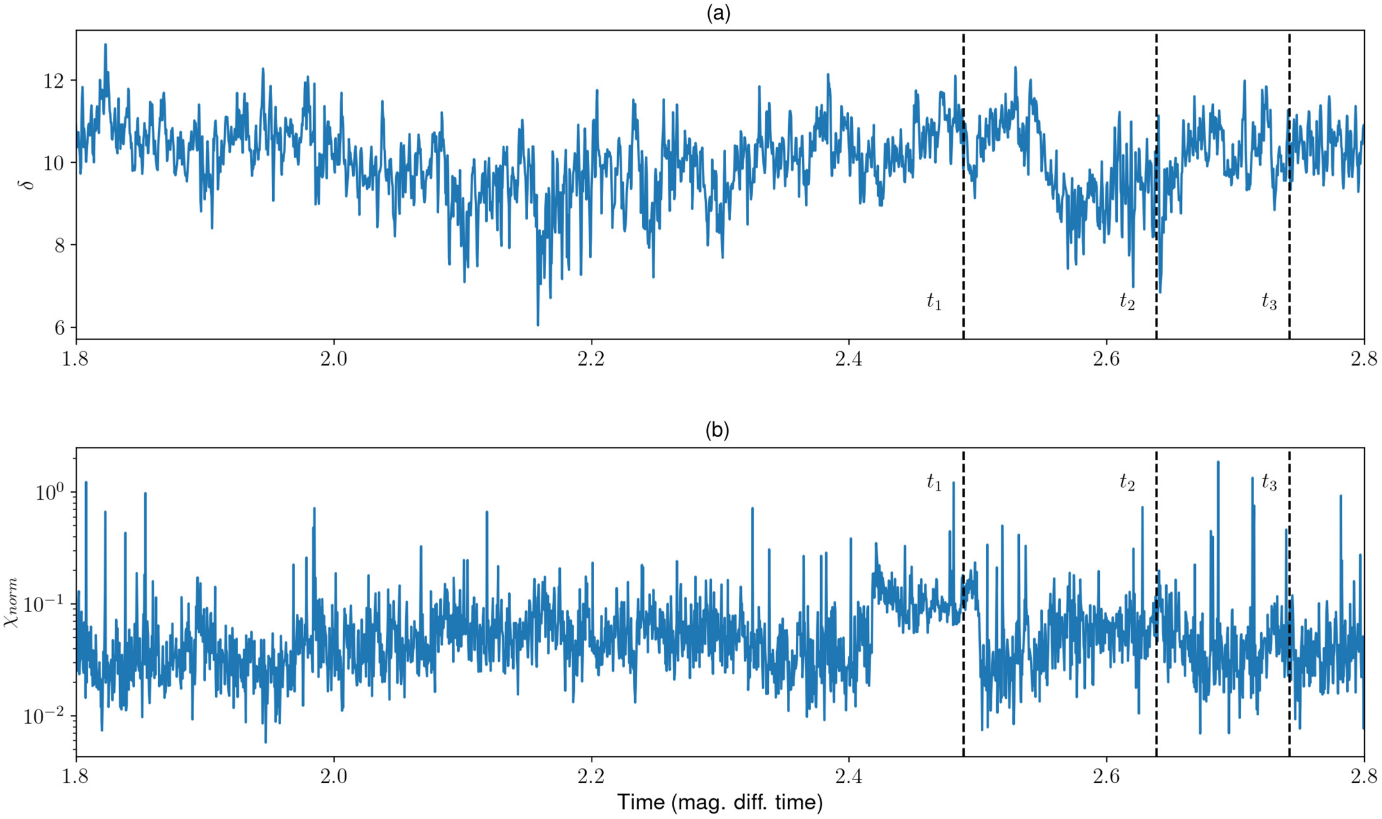

Fig. 5. (a) Strong fieldness (δ) and (b) χ_{norm} as a function of time for LEDT002. Time t_1: Before the reversal, t_2: During the reversal and t_3: After reversal.

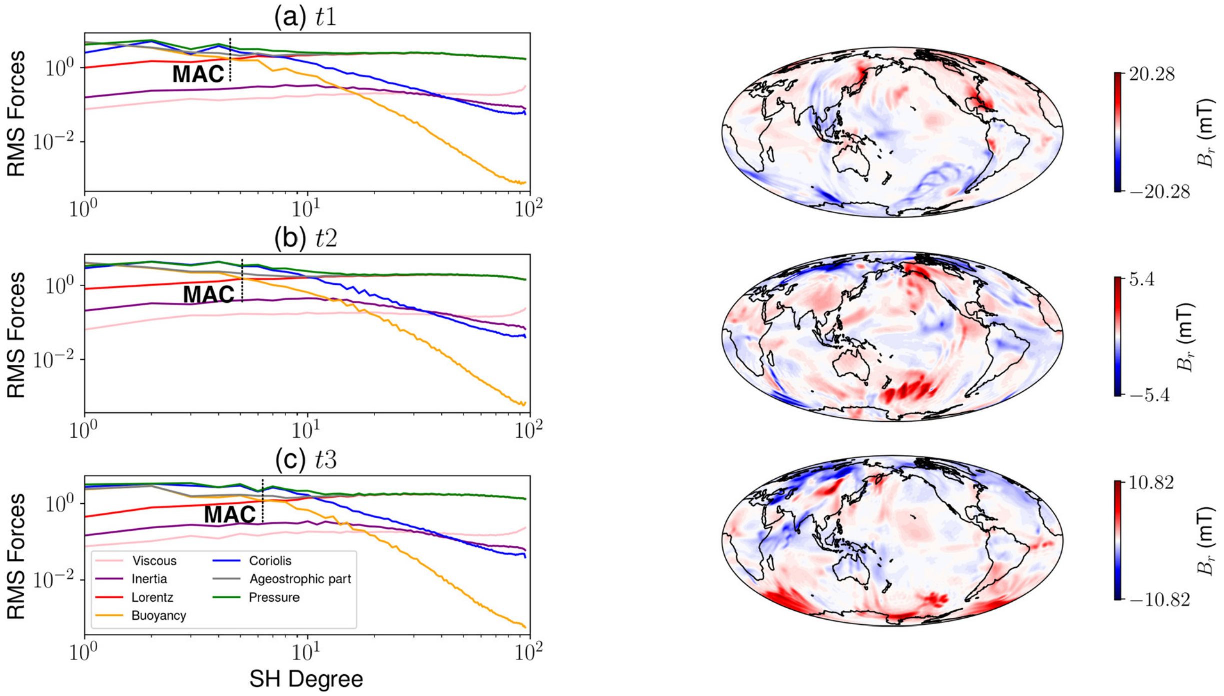

Fig. 6. Force balance spectra of bulk fluid layer (left) and the radial magnetic field at the CMB (right) during the polarity reversal for a case shown in Fig. 4. Time variations go from top to bottom (t_1 to t_3).

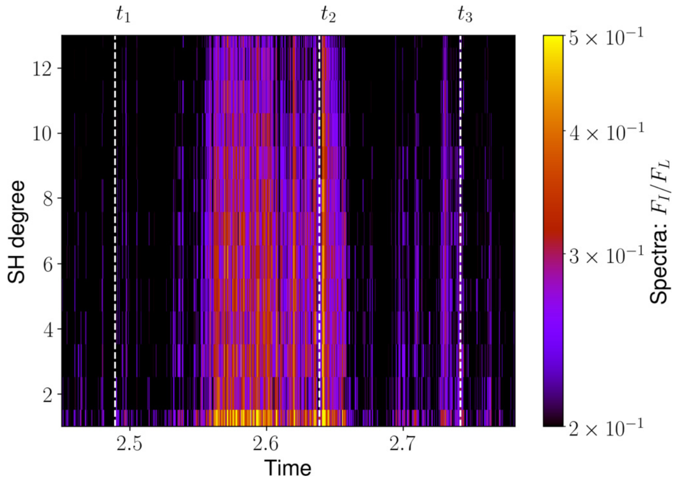

Fig. 7. Contour plot of the ratio of Lorentz and inertia force spectra as a function of time and spherical harmonic degree l. Dashed lines correspond to the times shown in Fig. 4.

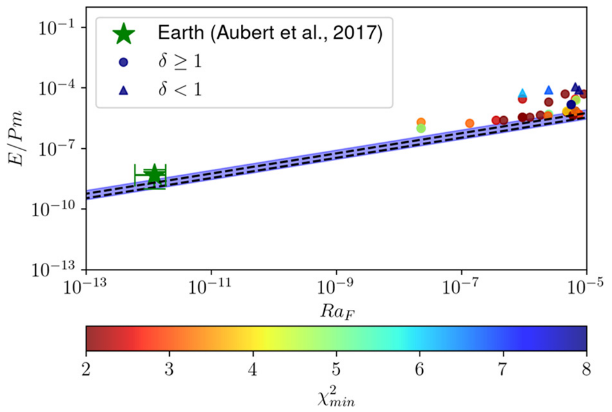

Fig. 8. All simulations (Table S1) plotted as functions of the flux Rayleigh Ra_F and ratio of Ekman to magnetic Prandtl numbers E/Pm. Filled colour indicates the total misfit of the compliance test taken at 400-yr time window corresponding to the minimum misfit. Circle: $\delta \geq 1$; Triangle: $\delta < 1$. Dashed lines are predicted relationships between Ra_F and E/Pm using Eq. (14) with the starting point of the path from this study and Aubert et al. (2017). The star with error bars determines the possible uncertainty on Earth values of E/Pm and Ra_F based on the range of heat flow across the core-mantle boundary (7 to 17 TW; Nimmo, 2015) and magnetic diffusivity (0.7 to 2 m^2/sec; Pozzo et al., 2013).

3.3. Asymptotic input parameters for Earth-like dynamos

We have shown that the dipolarity f_{dip} provides a reasonable proxy for dynamo simulations that comply with Earth's modern field morphology, magnetic Reynolds number and expected force balance. However, f_{dip} is an output of a geodynamo simulation and so it is of practical use to assess whether Earth-like dynamos (in the sense just described) can be predicted based on the input parameters, specifically E, Pm and Ra_F. Our simulation dataset uses moderate values of these input parameters that are far from Earth's core and so we also must consider whether the results may change as more realistic conditions are approached.

Fig. 8 plots all cases in Table S1 as a function of flux Rayleigh number Ra_F and E/Pm with filling colour showing the optimal χ^2 value in Fig. 2. Upper and lower dashed lines show the uni-dimensional paths used in this study (upper) and in Aubert et al. (2017) (lower), which are computed by Eq. (14). In our case, $Ra^*_0 = 120$ with $E_0 = 10^{-3}$ but $Ra^*_0 = 450$ for extrapolating the path provided by Aubert et al. (2017) with $E = 10^{-3}$. The difference between our path and Aubert et al.'s path is around a factor of four, corresponding the shaded region in Fig. 8. This difference is caused by the choice of starting condition of both paths. Fig. 8 shows that choosing input parameters close to those defined by a uni-dimensional path based on QG-MAC theory is a promising strategy for obtaining simulated fields that comply with Earth's modern field without needing to systematically sample parameter space. Note that Fig. 8 includes all of our simulations; however, due to the choice of input parameters, some cases overlap. The detailed information can be found in Table S1.

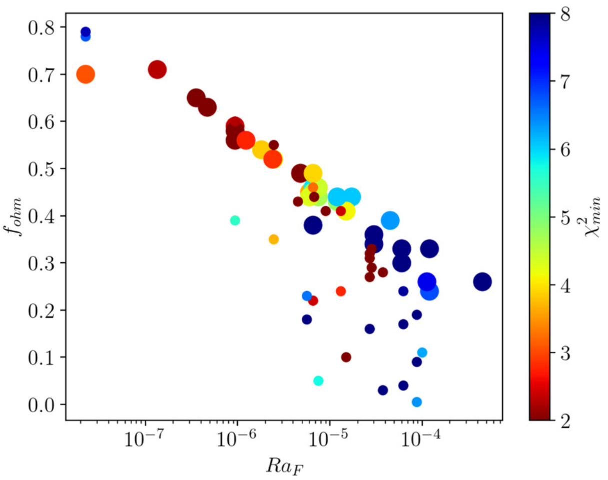

Fig. 9. Fraction f_{ohm} of the total dissipation that is Ohmic, plotted against flux Rayleigh number Ra_F. Colours show the minimum χ^2 morphological misfit taken across all 400-yr time windows.

Fig. 9 plots the fraction f_{ohm} of the total dissipation that is ohmic against the flux Rayleigh number Ra_F with minimum χ^2 based on 400-yr averages shown in colours. Simulations near the "path" parameters defined by Eq. (14) generally produce the highest f_{ohm} at a given Ra_F and correspond to the lower end of the χ^2 values. Decreasing Ra_F (towards Earth core conditions) leads to an increase in f_{ohm} (Aubert et al., 2017), but this does not imply that χ^2 remains low, as expected from Fig. 2.

4. Discussion

Our analysis of 67 numerical dynamos shows that simulations in QG-MAC balance generally provide good to excellent morphological agreement with the modern geomagnetic field within an intermediate range of dipolarity values that are broadly consistent with the range inferred for Earth's core independently of our simulation dataset (Davies et al., 2022). In fact, the majority of simulations exhibiting good or excellent compliance sit within the narrower range $0.55 \leq f_{dip} \leq 0.75$, demonstrating that dipolarity provides a strong constraint on dynamo behaviour. Conversely, simulations in QG-CIA balance (the only other dynamical regime to appear in our simulations) tend to produce low Rm, marginal- to non-compliant field morphologies, and dipolarities outside the range inferred by Davies et al. (2022). Below we consider how these results may depend on the methods used to compare simulations to observations and for estimating the dominant dynamics of the dynamo.

To compare simulated and observed fields we have relied on the compliance criteria of Christensen et al. (2010). The values of these criteria (and associated uncertainties) for Earth were selected by considering geomagnetic behaviour across the historical period (gufm-1; Jackson et al., 2000 and IGRF models https://www.ngdc.noaa.gov/IAGA/vmod/igrf.html)), as well as the Holocene (the CALS7k.2 model of Korte and Constable, 2005) and statistical models of the paleo-magnetic field spanning the last few million years. A new time-dependent spherical harmonic model for the last 100 kyrs (reviewed in Panovska et al., 2019) has become available, which can in principle be compared to numerical simulations. However, such comparisons must be conducted with care because of the differing spatio-temporal resolution of field models spanning different timescales. Panovska et al. (2019) show that the IGRF, CALS10k.2 Holocene model (Constable et al., 2016), and 100 kyr GGF model all give similar values for Z/NZ, O/E and FCF when truncated at degree 5, while AD/NAD varies by a factor of 4. Furthermore, all quantities are sensitive to the degree of truncation as Christensen et al. (2010) also noted. Future work is needed to critically evaluate different frameworks for comparing simulations to this new generation of time-dependent field models. Potential directions could utilize the PSV activity index (e.g. Panovska et al., 2019) or the form of the spatial power spectrum (Davies and Constable, 2014).

In addition to the compliance criteria, there are other characteristics of Earth's magnetic field that could be used to test numerical simulations (e.g. Davies and Constable, 2014; Sprain et al., 2019). Christensen et al. (2010) provide detailed arguments against adopting criteria based on the magnetic field strength, westward drift, or the apparently quasi-stationary high-latitude flux patches that are prominent in the modern field. Another consideration is the hemispheric pattern of secular variation that has been robustly revealed by satellite observations (e.g., Holme et al., 2011). This pattern has been reproduced in geodynamo simulations with heterogeneous boundary heat flow (Aubert et al., 2013; Mound et al., 2015) and has also been argued to arise from lateral variations in lower mantle electrical conductivity (Dumberry and More, 2020). Mound et al. (2015) proposed a measure of secular variation hemisphericity, H_{SV}, similar to the compliance criteria of Christensen et al. (2010). However, simulations with homogeneous boundary conditions tend to produce a poor match to Earth's H_{SV} (Aubert et al., 2013). Since we have focused on homogeneous models, we have not considered this criterion further, but note that it should be included as larger datasets containing both homogeneous and heterogeneous dynamos are produced.

On longer timescales, it is desirable to assess the compliance between simulations and the paleomagnetic field. Such comparisons cannot be conducted using the compliance criteria because spherical harmonic field models are not available for timescales greater than 100 kyrs, so other approaches such as the QPM (Quality Paleo-magnetic Model) framework are required (Sprain et al., 2019; Meduri et al., 2021). One challenge that we have demonstrated using a large simulation dataset is that reversals in QG-MAC dynamos are seldom observed, either because the simulations do not access the dipole-reversing regime or because they cannot be run for long enough to observe polarity changes. By combining large datasets such as used in Tassin et al. (2021) and the present paper, it may be possible to conduct systematic comparisons between dynamo models and the paleo-magnetic field.

To assess the dynamo force balance we have only discussed quantities as a function of spherical harmonic degree l. Schwaiger et al. (2019) obtained some simulations where the dominant force balance varied with radius, changing from QG-MAC in the bulk to QG-CIA near the outer boundary. We have verified that force balance spectra calculated by integrating over the bulk and by direct evaluation on the spherical surface corresponding to the base of the upper velocity boundary layer provide consistent estimates for the leading order and first order force balances. A further refinement that could be investigated in the future is to decompose the dependent variables and associated forces into mean and fluctuating components (Calkins et al., 2021). This approach allows to separately evaluate the relationship between the observed field and large- and small-scale force balances but requires a more complex analysis procedure that we have not attempted.

Future work should test our results with simulations carried out at more extreme values of E, Pm and Ra_F. Other simulation configurations should also be investigated. Our simulations employ the geophysically relevant no-slip velocity boundary conditions with fixed co-density flux on the inner and outer boundaries. We have also varied the ratio of internal to basal buoyancy driving, which is a significant unknown in the core (Davies and Gubbins, 2011), though only two configurations have been tested. Tassin et al. (2021) found a dependence of the compliance test results on buoyancy distribution by systematically varying the ratio of thermal to compositional driving. However, despite a different simulation setup and method for computing χ^2, their results reveal that excellent morphological semblance ($\chi^2 < 2$) is obtained almost exclusively in the QG-MAC regime (one outlying case has $M \approx 0.8$) and with f_{dip} in the range $0.55 - 0.8$, in good agreement with our findings. We therefore conclude that our results are not strongly sensitive to the buoyancy distribution in the parameter space that has been systematically studied to date.

Finally, we note that both f_{dip} and AD/NAD measure the degree of dipole dominance, and hence the intermediate f_{dip} regime we have identified could potentially be recast in terms of AD/NAD. We have chosen to use f_{dip} as it is a commonly reported diagnostic in dynamo studies. Our finding that QG-MAC balance, high *Rm* and low χ^2 simultaneously arise in a range of f_{dip} should enable existing simulations with these desirable properties to be easily identified.

5. Conclusions

We have run 67 numerical dynamo simulations to investigate links between the internal magnetohydrodynamic processes in Earth's core and the properties of the observable magnetic field. The order of forces in the dynamo have been estimated using the force balance spectra introduced by Aubert et al. (2017) and the morphological semblance between simulated and observed magnetic fields has been calculated using the χ^2 compliance criteria of Christensen et al. (2010). Our conclusions are as follows:

1. Both QG-MAC and QG-CIA dynamos can produce acceptable agreement with the modern geomagnetic field and so both the dynamo force balance and the characteristics of the surface field must be checked before making comparisons to Earth. However, the low χ^2 QG-CIA models appear close to the transition to QG-MAC balance, have low magnetic Reynolds number compared to Earth's core, and produce a dipolarity $\langle f_{dip} \rangle$ that is either too low or too high compared to the range $0.35 \leq f_{dip} \leq 0.75$ estimated by Davies et al. (2022) for the recent geomagnetic field. QG-CIA dynamos are therefore not representative of Earth's core dynamics.
2. Simulations that simultaneously produce Earth-like field morphology as defined by the compliance criteria, high magnetic Reynolds number, and a QG-MAC force balance all fall within the range of $\langle f_{dip} \rangle$ suggested by Davies et al. (2022). This range of $\langle f_{dip} \rangle$ appears to emerge in dynamo simulations conducted with input parameters that are close to those defined by unidimensional paths based on QG-MAC theory (Aubert et al., 2017).
3. A small number of reversing simulations have been identified in the range $0.35 \leq f_{dip} \leq 0.75$. These simulations maintain dominant QG-MAC balance during polarity transition, though the QG-MAC balance is strongly perturbed by inertia.

CRediT authorship contribution statement

Takashi Nakagawa: Conceptualization, Formal analysis, Investigation, Methodology, Software, Writing – original draft, Writing – review & editing. **Christopher J. Davies:** Conceptualization, Funding acquisition, Investigation, Methodology, Resources, Software, Writing – review & editing.

Declaration of competing interest

The authors declare that they have no known competing financial interests or personal relationships that could have appeared to influence the work reported in this paper.

Data availability

Analysed data and scripts for data analyses are available via the zenodo repository (https://doi.org/10.5281/zenodo.6479243). The Leeds numerical dynamo code is available via Github.

Acknowledgements

Numerical computations were performed on ARC4, part of the High Performance Computing facilities at the University of Leeds, UK and on ARCHER-2 of the UK National Supercomputing Service by UKRI and University of Edinburgh. This study is financially supported by NERC (grant NE/T012684/1) and NSF-NERC (grant NE/V009052/1). The authors thank C. Sprain, R. Bono, A. Biggin, D. Meduri and J. Mound for providing their simulation data for reanalysing force balance spectra and compliance test, and C. Constable for discussion on compliance test for field models.

Appendix A. Supplementary material

Supplementary material related to this article can be found online at https://doi.org/10.1016/j.epsl.2022.117752.

References

Aubert, J., 2019. Approaching Earth's core conditions in high-resolution geodynamo simulations. Geophys. J. Int. 219, S135–S151.

Aubert, J., Finlay, C.C., Fournier, A., 2013. Bottom-up control of geomagnetic secular variation by Earth's inner core. Nature 502, 219–223.

Aubert, J., Gastine, T., Fournier, A., 2017. Spherical convective dynamos in the rapidly rotating asymptotic regime. J. Fluid Mech. 813, 558–593.

Biggin, A.J., Bono, R.K., Meduri, M.G., Sprain, C.J., Davies, C.J., Holme, R., Doubrovine, P.V., 2020. Quantitative estimates of average geomagnetic axial dipole dominance in deep geological time. Nat. Commun. 11, 6100. https://doi.org/10.1038/s41467-020-19794-7.

Calkins, M.A., Orvedahl, R.J., Featherstone, N.A., 2021. Large-scale balances asymptotic scaling behaviour in spherical dynamos. Geophys. J. Int. 227, 1228–1245.

Cande, S., Kent, D.V., 1992. A new geomagnetic polarity time scale for the Late Cretaceous and Cenozoic. J. Geophys. Res., 13917–13951.

Christensen, U.R., 2018. Geodynamo models with a stable layer and heterogeneous heat flow at the top of the core. Geophys. J. Int. 215, 1338–1351.

Christensen, U.R., Aubert, J., 2006. Scaling properties of convection-driven dynamos in rotating spherical shells and application to planetary magnetic fields. Geophys. J. Int. 97 (114).

Christensen, U.R., Wicht, J., 2008. Models of magnetic field generation in partly stable planetary cores: applications to Mercury and Saturn. Icarus 196, 16–34.

Christensen, U.R., Aubert, J., Hulot, G., 2010. Conditions for Earth-like geodynamo models. Earth Planet. Sci. Lett. 296, 487–496.

Constable, C.G., Korte, M., Panovska, S., 2016. Persistent high paleosecular activity in Southern Hemisphere for at least 10,000 years. Earth Planet. Sci. Lett. 453, 78–86.

Davidson, P.A., 2013. Scaling laws of planetary dynamos. Geophys. J. Int. 195, 67–74.

Davies, C.J., Gubbins, D., 2011. A buoyancy profile for the Earth's core. Geophys. J. Int. 187, 549–563.

Davies, C.J., Constable, C.G., 2014. Insights from geodynamo simulations into long-term geomagnetic field behavior. Earth Planet. Sci. Lett. 404, 238–249.

Davies, C.J., Gubbins, D., Jimack, P.K., 2011. Scalability of pseudospectral methods for geodynamo simulations. Concurr. Comput., Pract. Exp. 23, 38–56.

Davies, C.J., Bono, R.K., Meduri, D.G., Aubert, J., Greenwood, S., Biggin, A.J., 2022. Dynamo constraints on the long-term evolution of Earth's magnetic field strength. Geophys. J. Int. 228, 316–336.

Dormy, E., Valet, J.-P., Courtillot, V., 2000. Numerical models of the geodynamo and observational constraints. Geochem. Geophys. Geosyst. 1. https://doi.org/10.1029/2000GC00062.

Dumberry, M., More, C., 2020. Weak magnetic field changes over the Pacific due to high conductance in lowermost mantle. Nat. Geosci. 13, 516–520.

Finlay, C.C., Kloss, C., Hammer, M.D., Toffner-Clause, L., Grayver, A., Kuvshinov, A., 2020. The CHAOS-7 geomagnetic field model and observed changes in the South Atlantic anomaly. Earth Planets Space 72, 156. https://doi.org/10.1186/s40623-020-01252-9.

Gastine, T., Aubert, J., Fournier, A., 2020. Dynamo-based limit to the extent of a stable layer atop Earth's core. Geophys. J. Int. 222, 1433–1448.

Holme, R., Olsen, N., Bairstow, F.L., 2011. Mapping geomagnetic secular variation at the core-mantle boundary. Geophys. J. Int. 186, 521–528.

Holme, R., 2015. Large-Scale Flow in the Core, second edition. Treatise on Geophysics, vol. 8, pp. 91–113.

Jackson, A., Jonkers, A.R.T., Walker, M.R., 2000. Four centuries of geomagnetic secular variation from historical records. Philos. Trans. R. Soc. Lond. A 358, 957–990.

King, E.M., Stellmach, S., Buffett, B., 2013. Scaling behaviour in Rayleigh-Bénard convection with and without rotation. J. Fluid Mech. 717, 449–471.

Korte, M., Constable, C.G., 2005. Continuous geomagnetic field models for the past 7 millennia. Geochem. Geophys. Geosyst. 6, Q02H16.

Korte, M., Brown, M.C., Panovska, S., Wardinski, I., 2018. Robust characteristics of the Laschamp and Mono Lake geomagnetic excursions: results from global field model. Front. Earth Sci. 7, 86. https://doi.org/10.3389/feart/2019.00086.

Masters, G., Laske, G., Bolton, H., Dziewonski, A., 2000. The relative behavior of shear velocity, bulk sound speed, and compressional velocity in the mantle: Implications for chemical and thermal structure. In: Earth's Deep Interior: Mineral Physics and Tomography Rom the Atomic to the Global Scale. In: Geophysical Monograph Series, vol. 117. American Geophysical Union, Washington DC, pp. 66–87.

Meduri, D.G., Biggin, A.J., Davies, C.J., Bono, R.K., Sprain, C.J., Wicht, J., 2021. Numerical dynamo simulations reproduce paleomagnetic field behavior. Geophys. Res. Lett. e2020GL090544.

Menu, M.D., Petitdemange, L., Galtier, S., 2020. Magnetic effects on field morphologies and reversals in geodynamo simulations. Phys. Earth Planet. Inter. 307, 106542.

Mound, J., Davies, C., Silva, L., 2015. Inner core translation and the hemispheric balance of the geomagnetic field. Earth Planet. Sci. Lett. 424, 148–157.

Nimmo, F., 2015. Energetics of the Core. Treatise on Geophysics, vol. 8, pp. 27–55.

Panovska, S., Korte, M., Constable, C.G., 2019. One hundred thousand years of geomagnetic field evolution. Rev. Geophys. 57, 1289–1337.

Pozzo, M., Davies, C., Gubbins, D., Alfé, D., 2013. Transport properties for liquid silicon-oxygen-iron mixtures at Earth's core condition. Phys. Rev. B 87. https://doi.org/10.1103/PhysRevB.87.014110.

Schwaiger, T., Gastine, T., Aubert, J., 2019. Force balance in numerical geodynamo simulations: a systematic study. Geophys. J. Int. 219, S101–S114.

Sheyko, A., Finlay, C.C., Jackson, A., 2016. Magnetic reversals from planetary dynamo waves. Nature 539, 551–554.

Sprain, C.J., Biggin, A.J., Davies, C.J., Bono, R.K., Meduri, D.G., 2019. An assessment of long duration geodynamo simulations using new paleomagnetic modeling criteria (Q_{PM}). Earth Planet. Sci. Lett. 526, 115758.

Tassin, T., Gastine, T., Fournier, A., 2021. Geomagnetic semblance and dipolar-multipolar transition in top-heavy double-diffusive geodynamo models. Geophys. J. Int. 226, 1897–1919.

Valet, J.-P., Fournier, A., 2016. Deciphering records of geomagnetic reversals. Rev. Geophys. 54, 410–446.

Wicht, J., Sanchez, S., 2019. Advances in geodynamo modelling. Geophys. Astrophys. Fluid Dyn. 113, 2–50.

Willis, A.P., Sreenivasan, B., Gubbins, D., 2007. Thermal core-mantle interaction: exploring regimes for 'locked' dynamo action. Phys. Earth Planet. Inter. 165, 83–92.

Yadav, R.K., Gastine, T., Christensen, U.R., Wolk, S.J., Poppenhaeger, K., 2016. Approaching a realistic force balance in geodynamo simulations. Proc. Natl. Acad. Sci. 113 (43), 12065–12070.

Further reading

Aubert, J., 2020. Recent geomagnetic variations and the force balance in Earth's core. Geophys. J. Int. 2020 (221), 378–393.